nature communications

Article

https://doi.org/10.1038/s41467-025-58024-w

Superconductivity and a van Hove singularity confined to the surface of a topological semimetal

Received: 30 July 2024

Accepted: 27 February 2025

Published online: 29 April 2025

Check for updates

Md Shafayat Hossain[1,9] ✉, Rajibul Islam[2,9], Zi-Jia Cheng[1,9], Zahir Muhammad[3,4,9], Qi Zhang[1], Zurab Guguchia[5], Jonas A. Krieger[5], Brian Casas[6], Yu-Xiao Jiang[1], Maksim Litskevich[1], Xian P. Yang[1], Byunghoon Kim[1], Tyler A. Cochran[1], Ilias E. Perakis[2], Thomas Hicken[5], Hubertus Luetkens[5], Fei Xue[2], Mehdi Kargarian[7], Weisheng Zhao[3], Luis Balicas[5,8] & M. Zahid Hasan[1] ✉

The interplay between topology and superconductivity generated great interest in condensed matter physics. Here, we unveil an unconventional two-dimensional superconducting state in the Dirac nodal line semimetal $ZrAs_2$ which is exclusively confined to the top and bottom surfaces within the crystal's *ab* plane. As a remarkable consequence, we present the first clear evidence of a Berezinskii–Kosterlitz–Thouless (BKT) transition occurring solely on a material's surface—specifically, $ZrAs_2$—unlike the inconsistent reports on $PtBi_2$, CaAgP, and $CaAg_{1-x}Pd_xP$. Furthermore, we find that these same surfaces also host a two-dimensional van Hove singularity near the Fermi energy. This leads to enhanced electronic correlations that contribute to the stabilization of superconductivity at the surface of $ZrAs_2$. The`surface-confined nature of the van Hove singularity and associated superconductivity, realized for the first time, allows exploring the interplay between low-dimensional quantum topology and superconductivity in a bulk material without resorting to the superconducting proximity effect.

Condensed matter fermions can acquire topological characteristics through their energy-momentum dispersions, characterized, for example, by Dirac/Weyl-like band crossings[1–5]. With the advent of topological insulators[1,2], a diverse array of topological phases came to light, spanning from confined zero-dimensional Dirac crossings in momentum space, as in Dirac and Weyl semimetals[4,5], to extended one-dimensional Dirac/Weyl lines or even loops, detected in nodal line semimetals[6–11]. These topological phases possess low-energy excitations or quasiparticles whose behavior mirrors those of relativistic particles, offering avenues for studying elusive phenomena in high-energy physics while materializing novel quantum effects not yet observed in known compounds[1–4]. In addition, linearly dispersing bands and related quasiparticles can be harvested to stabilize unique ground states, as exemplified by the topological insulators whose linearly dispersing surface bands were predicted to lead to interfacial triplet superconductivity when proximitized with conventional superconductors[12]. In general, and as exemplified by the transistor, interfacial states are of great relevance both scientifically and

[1]Laboratory for Topological Quantum Matter and Advanced Spectroscopy (B7), Department of Physics, Princeton University, Princeton, New Jersey, USA. [2]Department of Physics, University of Alabama at Birmingham, Birmingham, Alabama, USA. [3]National Key Laboratory of Spintronics, Hangzhou International Innovation Institute, Beihang University, Hangzhou, P.R. China. [4]Hefei Innovation Research Institute, School of Microelectronics, Beihang University, Hefei, P.R. China. [5]PSI Center for Neutron and Muon Sciences CNM, Villigen PSI, Switzerland. [6]National High Magnetic Field Laboratory, Tallahassee, Florida, USA. [7]Department of Physics, Sharif University of Technology, Tehran, Iran. [8]Physics Department, Florida State University, Tallahassee, FL, USA. [9]These authors contributed equally: Md Shafayat Hossain, Rajibul Islam, Zi-Jia Cheng, Zahir Muhammad. ✉e-mail: mdsh@princeton.edu; mzhasan@princeton.edu

technologically. Nevertheless, relatively little has been explored concerning interfaces involving the surface states in correspondence with bulk topological electronic states.

Recently, considerable attention has been focused on topological materials exhibiting electronic correlations and electronic order. Plausible ways to trigger correlations on surface states are via flatband-type drumhead states, as predicted for nodal line semimetals where a continuous line of Dirac nodes is observed[11,13–22], or the presence of van Hove singularities (vHss) near the Fermi level, as observed in Kagome superconductors[23–26]. In both scenarios, the drumhead states or vHss lead to pronounced peaks in the density of states, making these systems susceptible to the development of electronic order such as superconductivity, magnetism, or charge order[17–20,24–26]. Superconducting nodal line compounds, where superconductivity condenses from torus-shaped Fermi surfaces derived from the nodal lines, are predicted to harbor topological crystalline and second-order topological superconductivity[20]. Although several nodal line materials were recently discovered[27–41], with some even exhibiting superconductivity[39–41], no direct evidence for the unconventional nature of these superconducting states has been reported. The same applies to Kagome superconductors, where the intertwining between vHss and charge order with superconductivity has been suggested[26], but no clear consensus on the nature of the pairing mechanism has emerged[42–45]. Here, we present the discovery of two-dimensional superconductivity confined exclusively to the *ab*-plane of the nodal line semimetal, $ZrAs_2$. Notably, our momentum space spectroscopic studies of $ZrAs_2$ reveal two-dimensional vHs near the Fermi energy, confined to the same surfaces. Such proximity is likely to enhance electronic correlations contributing to the stabilization of superconductivity in the surface of $ZrAs_2$. Thus, $ZrAs_2$ potentially offers a natural solution to the stabilization of unconventional two-dimensional superconductivity in topological compounds, namely the coexistence between Dirac like quasiparticles and vHs at the surface state accompanied by a superconducting state.

Results

We begin our discussion with an examination of the electronic band structure of $ZrAs_2$. $ZrAs_2$ belongs to the nonsymmorphic space group *Pnma* (No. 62 D_{2h}^{16}) (Fig. 1a), which is known to host Dirac nodal lines[22,46]; the sample characterization data can be found in Supplementary Figs. 1– 3. Figure 1b illustrates the bulk and (001) surface projected Brillouin zone. In Fig. 1c, we present the electronic band structure (in the absence of spin-orbit coupling), revealing metallic behavior with both electron- and hole-like bands crossing the Fermi level. The partially filled bulk bands yield two hole-like Fermi surface pockets (FS_1^h and FS_2^h) and one electron-like Fermi surface pocket (FS_1^e) (Fig. 1d and e). This is consistent with our experimental findings exposing three peaks in the FFT spectrum from quantum oscillatory measurements (see Supplementary Information Section I and Supplementary Fig. 4, 5). Examining the energy bands along the X → Γ, Γ → Z, and X → U → Z directions, we identify multiple band crossings, labeled as NL1, NL2, NL3, and NL4 between the magenta and cyan bands and NL5 between the green and magenta bands as shown in Fig. 1c. The electronic band structure calculations characterize $ZrAs_2$ as a nodal line semimetal with four nodal loops protected by the mirror M_y and glide mirror (G_x and G_z) planes[22]. Figure 1f plots the nodal loops/lines in the k_x-k_y-k_z space, with black dots marking the nodal points along high-symmetry directions; the color bar shows the location of the nodes in energy. The distribution of the nodes (red lines) in the $k_z = 0$ plane is illustrated in Fig. 1g. A pair of concentric intersecting

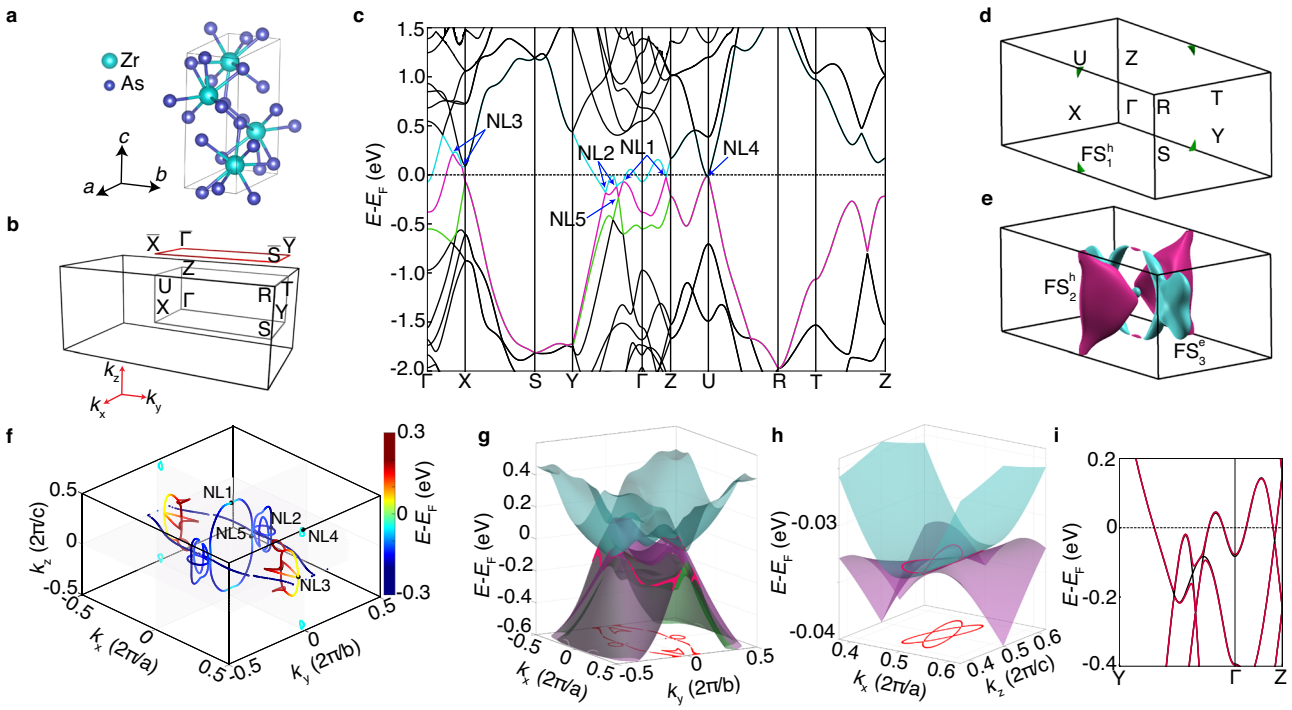

Fig. 1 | Electronic band structure of $ZrAs_2$ displaying nodal lines. a Crystal structure of $ZrAs_2$. **b** First Brillouin zone (surface and bulk) of $ZrAs_2$, highlighting its high symmetry points and the projection of the (001) surface. **c** Electronic band structure of $ZrAs_2$ obtained using first-principles calculations (without considering spin-orbit coupling) along high-symmetry lines. **d**, **e** Three-dimensional Fermi surface of $ZrAs_2$ displaying two hole-like (FS_1^h and FS_2^h) and one electron-like (FS_1^e) pockets. The color code corresponds to the bands shown in panel (**c**). **f** Nodal loops in the k_x-k_y-k_z space formed by the band crossings between green, magenta, and cyan bands in panels (**c**, **g**, **h**). Three-dimensional visualization of the electronic band crossings and the nodal lines or loops (red lines) within the $k_z = 0$ (panel **g**) and $k_y = 0$ planes near the U point (panel **h**). Bands are shown using the same color as in (**c**). The projection in E-$E_F = 0$ plane indicates the location of the nodes in momentum space. **i** Enlarged view of the band structure along the Y → Γ → Z direction, contrasting bands with (red) and without (black) spin-orbit coupling.

https://doi.org/10.1038/s41467-025-58024-w

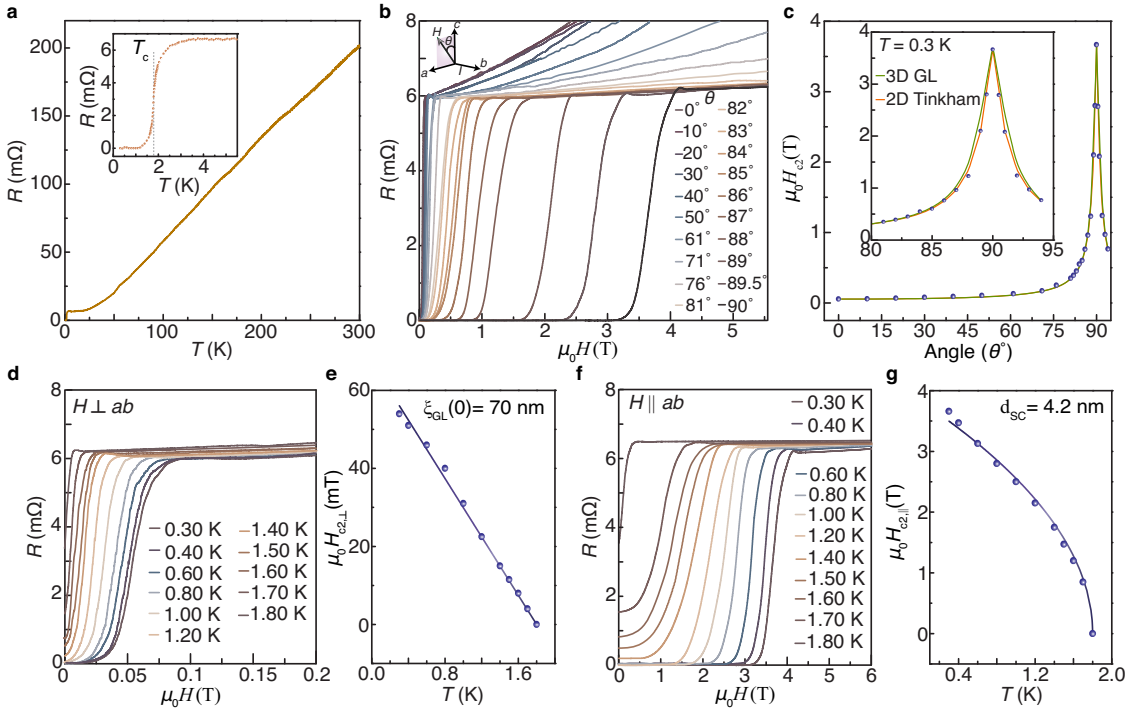

Fig. 2 | Superconducting instability in $ZrAs_2$. a Four-probe resistance (R) of a small $ZrAs_2$ single-crystal, exhibiting metallic behavior as a function of the temperature (T) before transitioning to a superconducting state at $T_c \simeq 1.8$ K. The inset depicts a magnified image of the resistance as a function of the temperature trace near T_c. **b** Resistance at $T \simeq 0.3$ K as a function of the magnetic field for different out-of-the-plane rotation angles (θ). The inset illustrates the direction of rotation, where θ represents the angle between the out-of-plane magnetic field and the c-axis of the crystal. **c** θ-dependence of the upper critical magnetic field ($\mu_0 H_{c2}$), defined as the field at which the resistance becomes half of its value in the normal state just above the transition. The orange and green curves represent the values expected from the Tinkham formula for a two-dimensional superconductor and the three-dimensional Ginzburg-Landau anisotropic mass model, respectively, considering the observed out-of-plane upper critical field ($\mu_0 H_{c2,\perp} = 0.056$ T) and in-plane upper critical field ($\mu_0 H_{c2,\parallel} = 3.66$ T). Inset: A magnified view of the same data near $\theta = 90^o$. The data show excellent agreement with the Tinkham formula while deviating from the three-dimensional Ginzburg-Landau anisotropic mass model, particularly near $\theta = 90^o$. **d** Resistance as a function of the out-of-plane magnetic field for different temperatures. **e** Temperature dependence of $\mu_0 H_{c2,\perp}$, displaying a linear dependence on T close to T_c. The dark blue line represents a fit to the Ginzburg-Landau model for two-dimensional superconductors, yielding an in-plane coherence length of $\xi_{GL}(0) \simeq 70$ nm. **f** Resistance as a function of the out-of-plane magnetic field for different temperatures. **g** Temperature dependence of $\mu_0 H_{c2,\parallel}$. The dark blue line depicts a fit to the Ginzburg-Landau model for two-dimensional superconductors, yielding a superconducting thickness of $d_{SC} \simeq 4.2$ nm.

coplanar ellipses from half-filled bands form a butterfly-like nodal loop around the U (π, 0, π) -point (Fig. 1h), as previously suggested[22].

To experimentally confirm the nodal features within the electronic band structure, we conducted angle-resolved photoemission spectroscopy (ARPES) measurements, which directly visualize the electronic bands. In Supplementary Fig. 6, we present ARPES data alongside an ab initio energy-momentum cut along the Y → Γ→Y path. ARPES energy-momentum (E-k) cut along the $\bar{Y} - \bar{\Gamma} - \bar{Y}$ path (Supplementary Fig. 6b) reveals two sets of band crossings: one located at $E - E_f = -0.29$ eV and another one near the Fermi level. These crossings align closely with the ab-initio calculations (Supplementary Fig. 6c), despite some bands being suppressed by matrix element effects or k_z broadening. These two crossings correspond to nodal lines NL5 and NL1, respectively. The excellent agreement between ARPES and the DFT calculations provides evidence for the existence of nodal lines in $ZrAs_2$. It is worth mentioning that, in the presence of spin-orbit coupling, the band crossings are lifted, leading to the emergence of a gap ranging from 2 to 58 meV (depending on the specific nodal feature), as depicted in Fig. 1j. The small gaps (e.g., 10 meV and 2 meV for NL1 and NL5, respectively) fall below the ARPES energy resolution (approximately 15 meV) and, therefore, cannot be observed under the presence of the k_z or extrinsic broadening and thus can be generally ignored[47,48]; see Supplementary Fig. 6c. Therefore, NL1 and NL5 can be effectively treated as a nodal line state under these conditions.

Having uncovered the band topology of $ZrAs_2$, we performed systematic electrical transport measurements. For this investigation, we selected a small, uniform, needle-shaped crystal and attached four electrical contacts on the ab-plane [(001) surface] of $ZrAs_2$ using silver epoxy; see Supplementary Information Section II and Supplementary Fig. 7 on how we determined the crystal plane prior to conducting the measurements. This configuration allows measurements of the longitudinal resistance (R) using the standard four-probe method. Figure 2a illustrates the temperature dependence of R. At elevated temperatures, R displays metallic behavior ($dR/dT > 0$), indicative of transport being dominated by phonon-scattering[49]. The residual resistivity ratio of approximately 35 indicates high sample quality and a significant variation in resistivity with temperature. Remarkably, the resistance undergoes a sudden drop to zero, marking the onset of superconductivity with a T_c of 1.8 K, which is the highlight of our investigation. Notice that Zr becomes a type-I superconductor below T_c of 0.6 K, while As only becomes superconducting under very high hydrostatic pressures[50,51]. Therefore, the observed superconducting state ought to be intrinsic to $ZrAs_2$. To investigate its characteristics, we probed the magnetoresistance well below T_c, at $T = 0.3$ K, while varying the magnetic field orientation,

https://doi.org/10.1038/s41467-025-58024-w

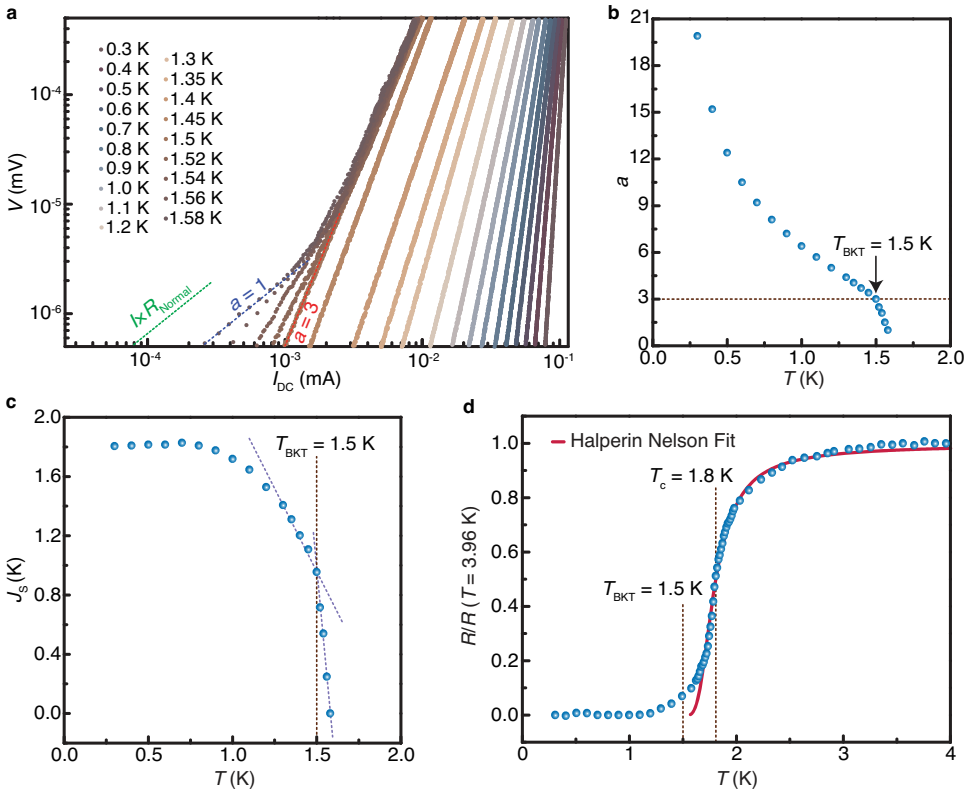

Fig. 3 | Observation of the Berezinskii–Kosterlitz–Thouless (BKT) transition. **a** Voltage (V)-current (I) characteristics acquired in the low-current regime, in a logarithmic scale, and for different temperatures. The red, blue, and green dashed lines represent $V \propto I^3$, $V \propto I$, and $V = I\,R_{\mathrm{Normal}}$, respectively. **b** Temperature dependence of the exponent $a(T) = 1 + \pi J_S(T)/T$ extracted from fitting the V-I data to $V \propto I^{a(T)}$. The BKT transition is characterized by $\pi J_S(T_{\mathrm{BKT}})/T_{\mathrm{BKT}} = 2$, leading to $a(T_{\mathrm{BKT}}) = 3$, the relation that defines T_{BKT}. The horizontal dashed line indicates the value $a = 3$. $a(T)$ as a function of T clearly reveals the BKT transition with $T_{\mathrm{BKT}} \simeq 1.5$ K. **c** Temperature dependence of the superfluid stiffness, J_S·J_S drops near T_c, as expected from the BCS theory. Above $T_{\mathrm{BKT}} \simeq 1.5$ K, the J_S decreases more rapidly with increasing T, as shown by the violet dashed lines serving as guides to the eye. **d** Temperature dependence of the resistance (blue circles), fitted to the Halperin–Nelson theory using the parameters $T_{\mathrm{BKT}} = 1.5$ K and $T_c = 1.8$ K. The Red curve represents the best fit.

spanning from the c-axis [001] ($\theta = 0^o$) to the [100] direction ($\theta = 90^o$) of $ZrAs_2$ (Fig. 2b). A crucial observation obtained from the magnetoresistance traces in Fig. 2b is the upper critical magnetic field (H_{c2}), corresponding to the field at which the resistance attains 50% of its normal state value. In Fig. 2c, we chart H_{c2} as a function of θ. As the magnetic field direction progresses from the out-of-plane ($\theta = 0^o$) to in-plane ($\theta = 90^o$) orientation with respect to the (001)-plane of $ZrAs_2$, the transition to the (field-induced) normal state systematically shifts to higher fields, with the maximum $\mu_0 H_{c2}(\theta)$ recorded at $\theta = 90^o$ (Fig. 3c). The in-plane $\mu_0 H_{c2}$ is determined to be approximately 3.66 T, which is 11% larger than the weak coupling Pauli (or Clogston–Chandrasekhar) paramagnetic limit, $\mu_0 H_p = 1.84 \times T_c$ T/K = 3.3 T for BCS superconductors[52,53]. This observation underscores a superconducting anisotropy, captured by the Tinkham formula governing the angular dependence of H_{c2} for a two-dimensional superconductor[54]: $\left|\frac{H_{c2}(\theta)\cos\theta}{H_{c2,\perp}}\right| + \left(\frac{H_{c2}(\theta)\sin\theta}{H_{c2,\parallel}}\right)^2 = 1$. Here, $\mu_0 H_{c2,\perp}$ and $\mu_0 H_{c2,\parallel}$ represent the upper critical magnetic fields for fields perpendicular and parallel to the sample plane, respectively. As depicted in Fig. 2c, our data aligns well with the Tinkham formula while revealing deviations (for near $\theta = 90°$) from the Ginzburg-Landau anisotropic mass model[52], which characterizes the angular dependence of $\mu_0 H_{c2}$ for a three-dimensional superconductor as: $\left(\frac{H_{c2}(\theta)\cos\theta}{H_{c2,\perp}}\right)^2 + \left(\frac{H_{c2}(\theta)\sin\theta}{H_{c2,\parallel}}\right)^2 = 1$. The conformity to the Tinkham formula is consistent with our observation of the (slight) violation of the Pauli limit. The θ-dependent measurements thus suggest that the superconductivity in $ZrAs_2$ is in the two-dimensional limit.

To gain further insights into the superconducting transition, we conducted systematic temperature-dependent measurements in Fig. 2d and e provide a visual representation of the acquired results when the magnetic field was applied perpendicularly to the $ZrAs_2$ (001) plane. It is worth noting that the superconducting transition progressively shifts to lower magnetic fields with increasing temperature. This evolution of the temperature-dependent out-of-plane upper critical magnetic fields ($\mu_0 H_{c2,\perp}$) is summarized in Fig. 2e. Given that the angular dependence of $\mu_0 H_{c2}(\theta)$ can be described by a two-dimensional superconductivity model, it is anticipated that $\mu_0 H_{c2,\perp}$ would exhibit a linear relationship with temperature close to T_c as given by the standard Ginzburg-Landau model for two-dimensional superconductors[54]: $\mu_0 H_{c2,\perp}(T) = \frac{\Phi_0}{2\pi\xi_{\mathrm{GL}}(0)^2}(1 - \frac{T}{T_c})$. Here $\xi_{\mathrm{GL}}(0)$ stands for the zero-temperature in-plane coherence length, Φ_0 is the magnetic flux quantum, and T_c is the critical temperature. Indeed, near T_c, $\mu_0 H_{c2,\perp}$ displays linear behavior as a function of T before dropping to zero at T_c as expected for two-dimensional superconductivity. By fitting the data, we estimate $\xi_{\mathrm{GL}}(0)$ to be 70 nm. We also examined the temperature-dependent superconducting transition with the magnetic field applied parallel to the sample ab plane. Figure 2f shows the corresponding traces, and Fig. 2f summarizes the result, illustrating the in-plane upper critical field $H_{c2,\parallel}$ as a function of temperature. Akin to $\mu_0 H_{c2,\perp}(T)$, $\mu_0 H_{c2,\parallel}(T)$ can be fitted to the standard Ginzburg-Landau model for

two-dimensional superconductors[54]: $\mu_0 H_{c2,||}(T) = \frac{\Phi_0\sqrt{3}}{\pi\xi_{GL}(0)d_{sc}}(1-\frac{T}{T_c})^{1/2}$ near T_c. From this fit, we extract a superconducting thickness $d_{SC} \approx 4.2$ nm, which is approximately 17 times smaller than $\xi_{GL}(0)$. Despite the good agreement with the fits to two-dimensional superconductivity, it should be noted that d_{SC} is much smaller (by at least 4 orders of magnitude) than the sample thickness but at least 4 times larger than the *c*-axis lattice constant of $ZrAs_2$, suggesting that its superconductivity could be confined to just 4 unit-cells at $ZrAs_2$ (001) plane.

The apparent two-dimensional superconductivity in $ZrAs_2$ cannot be directly attributed to the dimensionality of the bulk Fermi surface, which we directly probed through our quantum oscillatory experiments as depicted in Supplementary Figs. 4 and 5. The magnetoresistance traces displayed in Supplementary Figs. 4 and 5 reveal distinct $1/\mu_0 H$-periodic quantum oscillations (or the Shubnikov-de Haas effect). By analyzing the quantum oscillatory data (detailed in Supplementary Figs. 4 and 5, with a discussion in Supplementary Information Section I), we observe that while the quantum oscillatory frequencies (f_2 and f_3) display dependence on magnetic field orientation, neither conforms to the $1/\cos\theta$ dependency characteristic of two-dimensional Fermi surfaces. This observation implies that the carriers arising from these bulk Fermi surfaces are unlikely to contribute to the Cooper pairing mechanism. As discussed below, we therefore argue that the driving factor behind the superconductivity in $ZrAs_2$ is associated with paired charge carriers on the surface state of the *ab* plane.

Given that $ZrAs_2$ demonstrates a superconducting transition in resistivity measurements, one would anticipate the appearance of the Meissner effect. However, testing of multiple samples revealed that, despite the observable superconducting transition in the resistivity, the Meissner effect is absent down to 1.69 K (as shown in Supplementary Information Section III and Supplementary Fig. 8). Furthermore, as detailed in Supplementary Information Section IV and Supplementary Fig. 9, our muon spin relaxation (μSR) measurements in $ZrAs_2$ show no signature of a bulk superconducting state down to 0.04 K. The most likely explanation is that the superconductivity is confined to the surfaces of $ZrAs_2$. Magnetic DC susceptibility and μSR measurements require a large sample volume for the detection of the diamagnetic response associated with a superconducting transition. Consequently, if only the surface would superconduct and not the bulk of the material, such a state will not be captured by these techniques. This distinction likely explains why we did not observe signatures for superconductivity in $ZrAs_2$ from the magnetic susceptibility or μSR measurements since the superconductivity in this material is limited to its surface with the non-superconducting bulk contribution dominating the magnetic susceptibility and the μSR signals. Notably, the angular dependence of the $\mu_0 H_{c2}$ (θ) aligns with the possibility of superconductivity emerging solely in the *ab* plane of the orthorhombic crystal. Such a surface-confined superconducting state is expected to exhibit behavior characteristic of the two-dimensional limit, which is precisely what we observe in our measurements of $\mu_0 H_{c2}$ (θ), $\mu_0 H_{c2,\perp}(T)$, and $\mu_0 H_{c2,||}(T)$. It is also worth noting that a surface superconductor like $ZrAs_2$ is different from quasi-2D superconductors like $YBa_2Cu_3O_{7-\delta}$, which exhibit superconductivity in all layers, *i.e.*, in the bulk. Therefore, its superconductivity can be detected through magnetic susceptibility and μSR measurements.

The observation of two-dimensional superconductivity in a bulk single crystal sample lacking a quasi-two-dimensional Fermi surface, coupled with the absence of bulk superconductivity, strongly suggests that the pairing mechanism is exclusively driven by carriers on the surface state. This unique surface superconductivity fundamentally differs from three-dimensional superconductors, as it should give rise to the spontaneous emergence of vortices due to the Berezinskii–Kosterlitz–Thouless (BKT) transition in two-dimensions[55,56]. Through an examination of the voltage (*V*)- current (*I*) relationship obtained via electrical transport measurements across various temperatures, we uncover clear signatures of a BKT transition that reinforce the notion of the surface-confined nature of the superconducting state. As illustrated by Fig. 3a, at low temperatures, distinctive nonlinearities manifest in the *V*(*I*) characteristics, conforming to a temperature-dependent power law[57]: $V \propto I^{a(T)}$, where $a(T) = 1 + \pi J_S(T)/T$, and J_S represents the superfluid stiffness. The precise occurrence of the BKT transition is determined by the condition $\pi J_S(T_{BKT})/T_{BKT} = 2$, yielding $a(T_{BKT}) = 3$ and thereby defining the value of T_{BKT}. We identified such behavior in the *V*(*I*) characteristics, which are plotted in Fig. 3a and b, where a cubic power law is evident for $T \simeq 1.5$ K. Note that for the BKT transition in an infinite and homogeneous sample, a universal jump of $a(T)$ is anticipated at the BKT temperature (T_{BKT}), transitioning from $a(T>T_{BKT}) = 1$ to $a(T<T_{BKT}) = 3$. However, in practice, all samples inherently possess inhomogeneities or defects and are of a finite size. Consequently, the discontinuity in $a(T)$ at T_{BKT} is anticipated to broaden but must occur at a temperature between $T = T_c$ and $T = T_{BKT}$[57]. In $ZrAs_2$, we find that $a(T)$ decreases rather sharply with increasing temperature and falls to 1 within 0.08 K of T_{BKT}. Such a dramatic change in $a(T)$ is consistent with what one expects from the BKT transition.

For a consistency check, we also plot the superfluid stiffness $J_S(T)$ obtained from $\frac{T}{\pi}(a(T)-1)$ in Fig. 3c. We find that at low temperatures, $J_S(T)$ saturates, and elevated temperatures, $J_S(T)$ becomes smoothly suppressed as quasiparticles emerge when the temperature is raised, as qualitatively expected from the BCS theory; see Supplementary Information Section VI and Supplementary Fig. 4 for the BCS fitting results. Importantly, above T_{BKT}, $J_S(T)$ drops much rapidly as one would expect from the BKT transition. Note that the power dissipated in the sample corresponding to the traces presented in Fig. 3a is maximum 50 picowatts. Such a small power dissipation is unlikely to cause Joule heating of the sample.

Next, we scrutinized the temperature dependence of the resistance near the superconducting transition. Using the Halperin–Nelson theory[58], Benfatto et al. [57] formulated the temperature dependence of the resistance for $T \geq T_{BKT}$ as $\frac{R(T)}{R_N} = \frac{1}{1+A_{HN}\sin h^2\left(\sqrt{B_{HN}\frac{T_c-T_{BKT}}{T-T_{BKT}}}\right)}$. Here, R_N represents the normal state resistivity, B_{HN} stands for a dimensionless constant of the order of 1, and A_{HN} is a pre-factor. By fixing T_{BKT} at the value obtained from the *V*(*I*) characteristics, namely $T_{BKT} = 1.5$ K, we achieve a good fit to the experimental data (Fig. 3d). The good agreement with the Halperin–Nelson formula underscores that the superconducting state in $ZrAs_2$ resembles that of a pure superconducting state, as the formula assumes a homogenous superconducting state with no broadening in T_{BKT}. This observation is indeed in harmony with the high quality of the sample, as indicated by its substantial residual-resistivity ratio and the clear presence of quantum oscillatory phenomena (see Supplementary Information Section I). Importantly, it is worth emphasizing that, the BKT transition has previously been observed only in quasi-2D-layered superconductors and thin films[59–63]. Here, we argue that this work represents the first solid and complete study demonstrating the presence of superconductivity confined exclusively to the surface of any given compound.

In effect, surface superconductivity was previously claimed for CaAgP[64] and its Pd-doped version, as well as for $PtBi_2$[65]. For CaAgP and its Pd-doped variant, point contact spectroscopy would imply strong coupled, spin-triplet chiral superconducting pairing. However, such conclusions are at odds with the very small upper critical fields measured by the same authors, frequently seen in non-uniform, filamentary superconductors[66], thus suggesting that these hypotheses require

https://doi.org/10.1038/s41467-025-58024-w

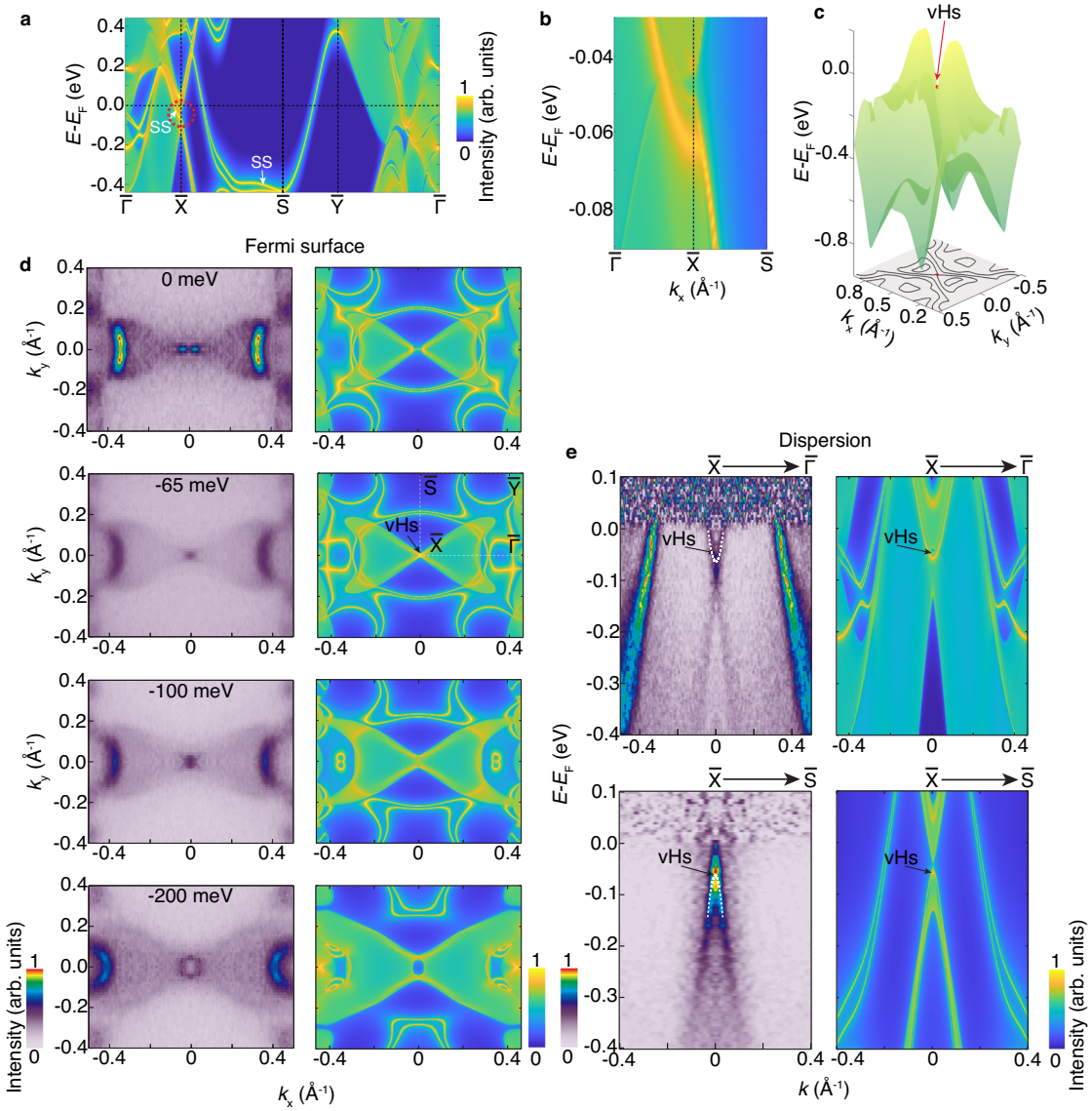

Fig. 4 | Surface van Hove singularity near the Fermi energy. a Ab-initio calculations (considering spin-orbit coupling) of the band structure projected onto the (001) surface, revealing the presence of surface states (SS), marked with arrows, and a van Hove singularity (vHs) at the $\bar{X}$ point. **b** Magnified view of the saddle point at the $\bar{X}$ point, marked with a red circle in panel (**a**). **c** Three-dimensional view of the surface state dispersion near the vHs at the $\bar{X}$ point on the k_x-k_y plane with k_z fixed at 0 Å. **d** Angle-resolved photoemission spectra (left column) and corresponding ab-initio calculations (considering spin-orbit coupling) illustrating the surface-projected constant energy contours at $E_b = 0$ eV,− 65 meV (where the vHs is located), − 100 meV, and 200 meV. For convenience, the coordinates of the $\bar{X}$ point are chosen to correspond to the (0, 0) coordinates. The photoemission spectroscopy results align with the calculated constant energy contours. The black arrow on the Fermi surface of the surface state indicates the location of the vHs, identified by the intersections among surface states. **e** Energy-momentum slices along the $\bar{\Gamma} - \bar{X} - \bar{\Gamma}$ and $\bar{S} - \bar{X} - \bar{S}$ directions acquired with photoemission spectroscopy (left column) and the (001) surface-projected calculation (right). The surface states (marked by white dashed parabolic bands) exhibit electron-like dispersion along $\bar{\Gamma} - \bar{X} - \bar{\Gamma}$ and hole-like dispersion along $\bar{S} - \bar{X} - \bar{S}$ the direction, forming a saddle point (marked by the black arrow) at the $\bar{X}$ point. For each binding energy, the energy-momentum cuts (panel **e**) are normalized at each binding energy to highlight band intensities near the Fermi level. The units in all the color bars shown are arbitrary units.

additional experimental confirmation. In ref. 64, and in contrast to our data, the surface superconducting transition does not lead to a zero-resistance state, while the surface superconducting state in CaAgP is found to be easily suppressed by the application of very small fields, i.e., $\mu_0 H = 31$ mT, in contrast to $ZrAs_2$ whose planar upper critical fields exceed $\mu_0 H = 3.5$ T at $T = 300$ mK. Notice that this is at odds with the authors' claims of spin-triplet *p*-wave superconductivity in Pd doped CaAgP, based on point contact spectroscopy, which would not be subjected to the Pauli limit. It is also at odds with the authors' claims in favor of strong coupled superconductivity, as suggested by the large ratio between the superconducting gap and the transition temperature, which the authors claim to substantially exceed the BCS ratio. As is well known for strongly correlated systems, e.g., heavy fermion superconductors, electronic correlations substantially renormalize orbital and Pauli upper critical fields towards very high values. Therefore, we find inconsistencies between their claims and observations. Notice that we also extract a large ratio between the superconducting gap Δ and T_c, *i.e.*, $\Delta/T_c = 2.685$, see Supplementary Information Section VI. But this is consistent with the measured upper critical fields perpendicular and along the planes that considerably exceed the Pauli limiting field $\mu_0 H_p = 1.84 \times T_c = 3.3$ T, as one reduces the temperature towards zero (Fig. 2). As for $PtBi_2$, the conclusion in favor of superconductivity below $T_c \approx 10$ K is based on the loss of the spectral weight of the Fermi arcs. Nevertheless, relatively thick exfoliated flakes from

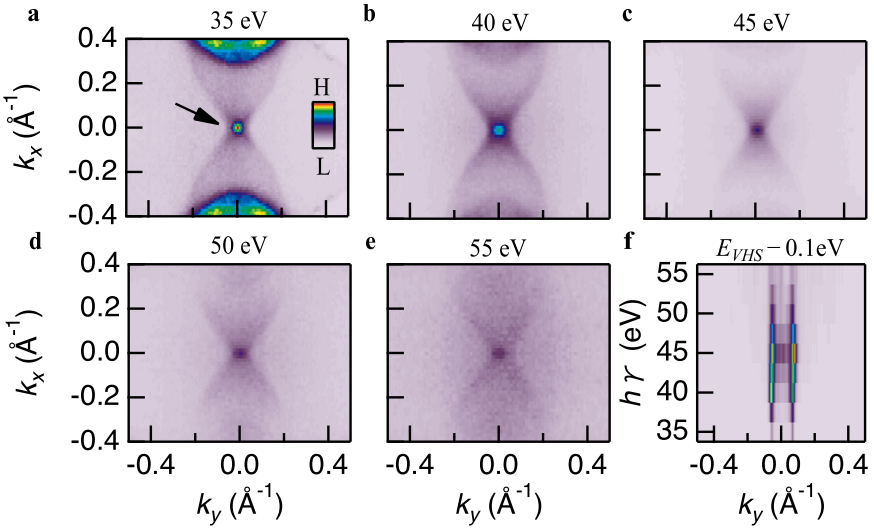

Fig. 5 | Photon energy dependence of the van Hove singularity (vHs) state at the $\bar{X}$ point. a–e Constant energy contours at the fixed energy of the vHs (E_{vHs}), measured at photon energies of 35, 40, 45, 50, and 55 eV, respectively. Note that the maps are symmetrized with respect to $k_x = 0$. **f** Photon energy dependence of the momentum distribution curves measured at $E_{vHs} - 0.1$ eV along the $\bar{S}$-$\bar{X}$-$\bar{S}$ direction. The contour of the vHs state remains unchanged across different photon energies, demonstrating its surface state nature. H and L in the color bar shown in panel (**a**) denote high and low intensities, respectively.

this type-I Weyl compound exhibit superconducting transitions well below 1 K, according to transport measurements[62]. Therefore, further work is required to elucidate the seemingly contradictory behavior of these superconductors. In contrast, our work on $ZrAs_2$ reveals a clear zero-resistance state, high planar upper critical fields, and a BKT-like superconducting transition, all in the absence of any evidence for bulk superconductivity, clearly suggesting a surface superconducting state.

The observation of surface-confined superconductivity in $ZrAs_2$ prompts us to explore the potential mechanisms that could stabilize such pairing in the surface state. To this end, we investigated the surface-projected Fermi surface and band structure. The ab initio calculations (incorporating spin-orbit coupling) of the surface state projected onto the (001) plane, where we observe the superconducting state, show termination-dependent surface state contribution. We consider the termination which matches our experimental data (see supplementary Information Section VIII and Supplementary Figs. 11 and 12). The calculations reveal a vHs located at the $\bar{X}$ point in the band corresponding to the surface state at approximately 65 meV below the Fermi level (see Fig. 4a, b). This saddle point is characterized by the crossing of the surface states at a constant energy contour (Fig. 4c). This observation is also evident in the three-dimensional view of the band structure of the surface state within the k_x-k_y plane, around the $\bar{X}$ point, as depicted in Fig. 4c. The saddle point, or vHs, results from the intersection of two symmetric pockets in the constant energy contours at the high symmetry $\bar{X}$-point.

To experimentally probe the vHs around the $\bar{X}$ point, we conducted further ARPES measurements. Figure 4d illustrates the evolution of the constant energy contours across consecutive energy slices; the left panels display the experimental results, while the right panels depict the corresponding ab initio calculations. As observed in Fig. 4d, two symmetry-related butterfly-wing-shaped states are separate at the Fermi level, with the apex of each pocket lying along the $\bar{\Gamma} - \bar{X}$ direction. As the energy is lowered to − 65 meV, the two states converge, ultimately leading to an intra-band intersection at the $\bar{X}$ point, thus forming a vHs. Further changes in energy towards − 100 meV and − 150 meV reveal butterfly-like features and their intersecting section near the $\bar{X}$ point becomes hole-like. The presence of vHs in the surface state is also evident in the energy-momentum slices along the $\bar{\Gamma} - \bar{X} - \bar{\Gamma}$ and $\bar{S} - \bar{X} - \bar{S}$ directions. Figure 4e illustrates these results, showcasing the energy-momentum dispersion spectra on the (001) surface projected ab initio calculations. Notably, the (001) surface state displays an electron-like dispersion along the $\bar{\Gamma} - \bar{X} - \bar{\Gamma}$ direction and a hole-like dispersion along the $\bar{S} - \bar{X} - \bar{S}$ direction, thus highlighting the formation of a saddle point at the $\bar{X}$ point. Therefore, our ARPES spectra combined with ab initio calculations unveil a vHs around the $\bar{X}$ point in the electronic surface bands of the (001) plane, precisely where we observe the two-dimensional superconducting state.

To further distinguish between surface and bulk contributions to the observed vHs, we performed a detailed photon-energy-dependent ARPES study. Figure 5 summarizes our results. Our analysis reveals that at the binding energy $E_B = E_{vHs}$, the contour of the vHs state near the $\bar{X}$ point remains consistent across the photon energy range studied (35–55 eV), as illustrated in Fig. 5f. Furthermore, the peaks in the momentum distribution curves at $E_B = E_{vHs} - 0.1$ eV, corresponding to the hole dispersion of the VHS state along the $\bar{S}$-$\bar{X}$-$\bar{S}$ direction, show no variation with photon energy, as illustrated in Fig. 5f. In contrast, the bulk state near the $\bar{\Gamma}$ point shows significant variation with photon energy, underscoring the distinct behavior inherent to bulk states. This absence of photon energy dependence for the vHs state suggests that it results from a surface state, as surface states are independent of photon energy, unlike bulk states. We refer the readers Supplementary Fig. 13a–c for additional results supporting that the vHs is formed by the surface state.

The presence of a vHs in the k_x-k_y-plane within the first Brillouin zone indicates an enhanced density of states at − 65 meV, which is slightly below the Fermi energy (see Supplementary Figs. 14 for the ARPES results and 15 for the ab-initio calculations) within that plane. Supplementary Fig. 14 presents energy distribution curves along two orthogonal directions passing through the $\bar{X}$ point. We find that the peak observed at the top band along the $\bar{S} - \bar{X} - \bar{S}$ direction aligns with the bottom of the band along the $\bar{\Gamma} - \bar{X} - \bar{\Gamma}$ path, forming a two-dimensional saddle point. This saddle point in the surface state dispersion naturally results in vHs, owing to the inevitable divergence of the density of states at the saddle point of a two-dimensional electronic state[67,68]. The corresponding increased density of states, which can be further explored via future tunneling measurements, has the potential to induce electronic order, such as superconductivity. Our transport experiments, presented in Figs. 2 and 3, reveal that the

superconducting state is confined within the *ab*-plane, which is directly connected with the k_x-k_y-plane in the first Brillouin zone where the vHs is located (Fig. 4). Hence, it is likely that the vHs, and concomitant enhanced density of states, play a pivotal role in stabilizing the superconducting state on the same surface.

Discussion

Our discovery carries several implications: first, it establishes a convenient material platform for investigating superconductivity on the surfaces of a topological material, with this being important for the field of topological superconductivity[12,69]. Second, it provides a material foundation for exploring the interplay between vHs and superconductivity at low dimensions (see our theory discussion in Supplementary Information Sections V–VII for possible pairing symmetries for the nontrivial topology of the superconducting state), paving the way for the discovery of unconventional quasiparticles such as Majorana fermions. We remark that our fittings of the superfluid stiffness yield a large ratio between the gap and the superconducting transition temperature, pointing to the strongly coupled and likely unconventional nature of the superconducting pairing. This is consistent with strong electronic correlations at the surface, as expected from the presence of vHs. The unprecedented surface-confined nature of both the vHs and superconductivity opens avenues for studying low-dimensional physics, akin to the correlation-induced low-dimensional superconductivity observed in twisted bilayer graphene, but in bulk materials. Third, it provides a strategy, beyond the proximity effect, for observing potentially unconventional superconductivity at the surface of topologically non-trivial compounds. Finally, given that these quantum phenomena emerge at the surface of a topological material, they are expected to exhibit robustness against local perturbations, thus exhibiting potential for applications in quantum devices that harness surface-confined superconductivity.

Methods

Synthesis of $ZrAs_2$ single crystals

$ZrAs_2$ single crystals were synthesized through a two-step chemical vapor transport (CVT) technique[70]. High-purity precursors, consisting of Zirconium (Zr) with a purity of 99.98% and Arsenic (As) foil with a purity of 99.99%, were combined in a stoichiometric ratio of 1:2. The mixture was introduced along with iodine as a transport agent into quartz tubes under a vacuum pressure of 5×10^{-4} Torr. The quartz tubes were subsequently placed in a two-temperature commercial CVT setup, maintaining the lower and higher temperatures at 850 °C and 750 °C, respectively, for a continuous five-day period. The reaction was then gradually cooled down to room temperature at a rate of 100 °C/h, resulting in the formation of polycrystalline samples. The obtained polycrystals were finely ground and then subjected to the same CVT process using iodine as the transport agent. This process was conducted with the same temperature gradient for a duration of two weeks. Following this, needle-like single crystals of typical dimensions ranging from 0.5 to 1 mm (in length) were successfully obtained in the hotter end (Supplementary Fig. 1a). The crystallographic orientation and structure of the single crystals were determined using Powder X-ray diffraction (XRD) measurements (Supplementary Fig. 1b). The XRD patterns were matched with the DB Card No: 01-079-6540 (ICDD (PDF-4 + 2020 RDB)). The XRD data further confirmed the Cotunnite mineral structure of $ZrAs_2$, crystallizing in the orthorhombic Pnma (62) space group with lattice parameters a = 6.8016(10) Å, b = 3.6889(5) Å, and c = 9.0305(13) Å.

We have also performed energy-dispersive X-ray spectroscopy (EDS) measurements on the $ZrAs_2$ crystals to determine the exact stoichiometric ratio of Zr and As in the grown crystals. The results are summarized in Supplementary Figs. 2 and 3 and Supplementary Tables 1 and 2. Various portions of the crystal, shown in Supplementary Fig. 2a, were examined to estimate the chemical composition. The selected area revealed that, except for carbon (used to adhere the sample to the holder), only Zr and As peaks are visible in the EDS spectrum. We further tested different points and areas to determine the stoichiometric ratio of the elements in the compound, as detailed in Supplementary Tables 1 and 2. Supplementary Table 1 presents the specific ratios found in different parts, while Supplementary Table 2 displays the calculated mean values derived from Supplementary Table 1. These results unequivocally confirm the exact stoichiometric ratio of Zr to As as 1:2.

First-principles calculations

The electronic structure calculations were conducted using the projector augmented wave method within the density functional theory framework, employing the VASP package[71]. A plane-wave energy cutoff of 650 eV was utilized for the study. The generalized gradient approximation (GGA) method served as the exchange-correlation functional[72]. Electronic band structure calculations were performed using a $6 \times 12 \times 4$ Monkhorst-Pack k-mesh, with self-consistent incorporation of spin-orbit coupling. The VASPWANNIER90 interface was utilized, utilizing s and d-orbitals of Zr atoms and p-orbitals of As atoms, to generate a tight-binding Hamiltonian without employing the procedure for maximizing localization[73,74]. The calculation of the surface state was performed using the semi-infinite Green's function approach integrated into the WannierTools[75,76]. We performed all the calculations with spin-orbit coupling except for the data shown in Fig. 1c–h.

Angle-resolved photoemission spectroscopy measurements

The angle-resolved photoemission spectroscopy measurements were performed at the beamline BL21_ID (ESM) of National Synchrotron Light Source II (NSLS II). The samples were cleaved under ultra-high vacuum conditions and measured at T = 10 K. The data were obtained using a photon energy of 40 eV with p polarization. The energy and momentum resolutions are better than 15 meV and 0.01 $Å^{-1}$, respectively. Due to the strong interatomic bonds in $ZrAs_2$, cleaving this material is particularly challenging, and the resulting flat terraces that yield sharp ARPES spectra are typically around 100×100 μm^2 in size. To overcome this challenge, we cleaved multiple samples and utilized a small beam size ($<30 \times 50$ μm^2) at BL21 to investigate the band structure within a single flat region.

Transport measurements

Low-field transport measurements (presented in Figs. 2 and 3) were conducted using an Oxford Heliox system, which has a base temperature of 0.3 K and a maximum magnetic field capability of 8 T. To obtain the temperature-dependent quantum oscillations data (presented in Supplementary Fig. 4), we used the WM5 water-cooled magnet generating magnetic fields up to 35 T at the Steady High Magnetic Field Facilities of the High Magnetic Field Laboratory, Chinese Academy of Sciences in Hefei, China. On the other hand, for angle-dependent magnetoresistance measurements acquired at T = 5 K (presented in Supplementary Fig. 5), we utilized a standard 4He cryostat and magnetic fields up to approximately 28.3 T.

Data availability

All data needed to evaluate the conclusions in the paper are present in the paper. Additional data are available from the corresponding authors upon request.

References

1. Hasan, M. Z. & Kane, C. L. Colloquium: Topological insulators. *Rev. Mod. Phys.* **82**, 3045 (2010).
2. Qi, X.-L. & Zhang, S.-C. Topological insulators and superconductors. *Rev. Mod. Phys.* **83**, 1057 (2011).

3. Volovik, G. E. *The Universe in a Helium Droplet* (Oxford Univ. Press, 2007).
4. Burkov, A. Topological semimetals. *Nat. Mater* **15**, 1145–1148 (2016).
5. Armitage, N. P., Mele, E. J. & Vishwanath, A. Weyl and Dirac semimetals in three-dimensional solids. *Rev. Mod. Phys.* **90**, 015001 (2018).
6. Burkov, A. A., Hook, M. D. & Balents, L. Topological nodal semimetals. *Phys. Rev. B* **84**, 235126 (2011).
7. Kim, Y., Wieder, B. J., Kane, C. L. & Rappe, A. M. Dirac line nodes in inversion-symmetric crystals. *Phys. Rev. Lett.* **115**, 036806 (2015).
8. Fang, C., Chen, Y., Kee, H.-Y. & Fu, L. Topological nodal line semimetals with and without spin-orbital coupling. *Phys. Rev. B* **92**, 081201 (2015).
9. Weng, H. et al. Topological node-line semimetal in three-dimensional graphene networks. *Phys. Rev. B* **92**, 045108 (2015).
10. Fang, C., Weng, H., Dai, X. & Fang, Z. Topological nodal line semimetals. *Chin. Phys. B* **25**, 117106 (2016).
11. Bzdušek, T., Wu, Q., Rüegg, A., Sigrist, M. & Soluyanov, A. A. Nodal-chain metals. *Nature* **538**, 75 (2016).
12. Fu, L. & Kane, C. L. Superconducting proximity effect and majorana fermions at the surface of a topological insulator. *Phys. Rev. Lett.* **100**, 096407 (2008).
13. Bian, G. et al. Drumhead surface states and topological nodal-line fermions in $TlTaSe_2$. *Phys. Rev. B* **93**, 121113 (2016).
14. Chan, Y.-H., Chiu, C.-K., Chou, M. Y. & Schnyder, A. P. Ca_3P_2 and other topological semimetals with line nodes and drumhead surface states. *Phys. Rev. B* **93**, 205132 (2016).
15. Pezzini, S. et al. Unconventional mass enhancement around the Dirac nodal loop in ZrSiS. *Nat. Phys.* **14**, 178–183 (2017).
16. Huh, Y., Moon, E.-G. & Kim, Y.-B. Long-range Coulomb interaction in nodal-ring semimetals. *Phys. Rev. B* **93**, 035138 (2016).
17. Liu, J. & Balents, L. Correlation effects and quantum oscillations in topological nodal-loop semimetals. *Phys. Rev. B* **95**, 075426 (2017).
18. Roy, B. Interacting line-node semimetal and spontaneous symmetry breaking. *Phys. Rev. B* **96**, 041113 (2017).
19. Wang, Y. & Nandkishore, R. M. Topological surface superconductivity in doped Weyl loop materials. *Phys. Rev. B* **95**, 060506 (2017).
20. Shapourian, H., Wang, Y. & Ryu, S. Topological crystalline superconductivity and second-order topological superconductivity in nodal-loop materials. *Phys. Rev. B* **97**, 094508 (2018).
21. Lim, L.-K. & Moessner, R. Pseudospin vortex ring with a nodal line in three dimensions. *Phys. Rev. Lett.* **118**, 016401 (2017).
22. Zhou, X. et al. Novel family of topological semimetals with butterflylike nodal lines. *Phys. Rev. B* **104**, 125135 (2021).
23. LaBollita, H. & Botana, A. S. Tuning the Van Hove singularities in AV_3Sb_5 (A = K, Rb, Cs) via pressure and doping. *Phys. Rev. B* **104**, 205129 (2021).
24. Kang, M. et al. Twofold van Hove singularity and origin of charge order in topological kagome superconductor CsV_3Sb_5. *Nat. Phys.* **18**, 301–308 (2022).
25. Hu, Y. et al. Rich nature of Van Hove singularities in Kagome superconductor CsV3Sb5. *Nat. Commun.* **13**, 2220 (2022).
26. Luo, Y. et al. A unique van Hove singularity in kagome superconductor $CsV_{3-x}Ta_xSb_5$ with enhanced superconductivity. *Nat. Commun.* **14**, 3819 (2023).
27. Yu, R. et al. Topological node-line semimetal and Dirac semimetal state in antiperovskite Cu_3PdN. *Phys. Rev. Lett.* **115**, 036807 (2015).
28. Bian, G. et al. Topological nodal-line Fermions in spin-orbit metal $PbTaSe_2$. *Nat. Commun.* **7**, 10556 (2016).
29. Schoop, L. M. et al. Dirac cone protected by non-symmorphic symmetry and three-dimensional Dirac line node in ZrSiS. *Nat. Commun.* **7**, 11696 (2016).
30. Wu, Y. et al. Dirac node arcs in $PtSn_4$. *Nat. Phys.* **12**, 667–671 (2016).
31. Neupane, M. et al. Observation of topological nodal fermion semimetal phase in ZrSiS. *Phys. Rev. B* **93**, 201104 (2016).
32. Li, R. et al. Dirac node lines in pure alkali earth metals. *Phys. Rev. Lett.* **117**, 096401 (2016).
33. Xu, Y. & Zhang, C. Dirac and Weyl rings in three-dimensional cold-atom optical lattices. *Phys. Rev. A* **93**, 063606 (2016).
34. Topp, A. et al. Surface floating 2D bands in layered nonsymmorphic semimetals: ZrSiS and related compounds. *Phys. Rev. X* **7**, 041073 (2017).
35. Zhang, X., Yu, Z.-M., Sheng, X.-L., Yang, H. Y. & Yang, S. A. Coexistence of four-band nodal rings and triply degenerate nodal points in centrosymmetric metal diborides. *Phys. Rev. B* **95**, 235116 (2017).
36. Huang, H., Jin, K.-H. & Liu, F. Topological nodal-line semimetal in nonsymmorphic Cmce -phase Ag_2S. *Phys. Rev. B* **96**, 115106 (2017).
37. Jiao, Y. et al. First-principles prediction of spin-polarized multiple dirac rings in manganese fluoride. *Phys. Rev. Lett.* **119**, 016403 (2017).
38. Li, S. et al. Nonsymmorphic-symmetry-protected hourglass Dirac loop, nodal line, and Dirac point in bulk and monolayer X_3SiTe_6 (X = Ta, Nb). *Phys. Rev. B* **97**, 045131 (2018).
39. Shang, T. et al. Spin-triplet superconductivity in Weyl nodal-line semimetals. *Npj Quantum Mater.* **7**, 35 (2022).
40. Li, L. et al. Superconductivity in the nodal-line compound $La_3Pt_3Bi_4$. Phys. *Rev. Res.* **4**, L032004 (2022).
41. Shang, T. et al. Unconventional superconductivity in topological Kramers nodal-line semimetals. *Sci. Adv.* **8**, eabq6589 (2022).
42. Mu, C. et al. S-Wave Superconductivity in kagome metal CsV_3Sb_5 revealed by $^{121/123}$Sb NQR and ^{51}V NMR measurements. *Chin. Phys. Lett.* **38**, 077402 (2021).
43. Duan, W. et al. Nodeless superconductivity in the kagome metal CsV_3Sb_5. *Sci. China Phys. Mech. Astron.* **64**, 107462 (2021).
44. Gupta, R. et al. Microscopic evidence for anisotropic multigap superconductivity in the CsV_3Sb_5 kagome superconductor. *Npj Quantum Mater.* **7**, 49 (2022).
45. Xu, H.-S. et al. Multiband Superconductivity with Sign-Preserving Order Parameter in Kagome Superconductor CsV_3Sb_5. *Phys. Rev. Lett.* **127**, 187004 (2021).
46. Mozaffari, S. Multiple Dirac nodes and symmetry protected Dirac nodal line in orthorhombic α -RhSi. *Phys. Rev. B* **102**, 115131 (2020).
47. Fu, B.-B. et al. Dirac nodal surfaces and nodal lines in ZrSiS. *Sci. Adv.* **5**, eaau6459 (2019).
48. Lou, R. et al. Experimental observation of bulk nodal lines and electronic surface states in ZrB_2. *Npj Quantum Mater.* **3**, 43 (2018).
49. Kawamura, T. & Sarma, S. D. Phonon-scattering-limited electron mobilities in $Al_xGa_{1-x}As$/GaAs heterojunctions. *Phys. Rev. B* **45**, 3612 (1992).
50. Chen, A. L. et al. Superconductivity in arsenic at high pressures. *Phys. Rev. B* **46**, 5523 (1992).
51. Tsuppayakorn-aek, P. et al. The high-pressure superconducting phase of arsenic. *Sci. Rep.* **8**, 3026 (2018).
52. Chandrasekhar, B. S. A note on the maximum critical field of high-field superconductors. *Appl. Phys. Lett.* **1**, 7–8 (1962).
53. Clogston, A. M. Upper limit for critical field in hard superconductors. *Phys. Rev. Lett.* **9**, 266–267 (1962).
54. Tinkham, M. *Introduction to Superconductivity Second Edition*. (McGraw-Hill, New York, 1996).
55. Berezinskii, V. L. Destruction of long-range order in one-dimensional and two-dimensional systems possessing a continuous symmetry group. II. quantum systems. *Sov. Phys.-JETP* **34**, 610 (1972).
56. Kosterlitz, J. M. & Thouless, D. J. Ordering, metastability and phase transitions in two-dimensional systems. *J. Phys. C Solid State Phys.* **6**, 1181–1203 (1973).

57. Benfatto, L., Castellani, C. & Giamarchi, T. Broadening of the berezinskii-kosterlitz-thouless superconducting transition by inhomogeneity and finite-size effects. *Phys. Rev. B* **80**, 214506 (2009).
58. Halperin, B. I. & Nelson, D. R. Resistive transition in superconducting films. *J. Low Temp. Phys.* **36**, 599–616 (1979).
59. Baity, P. G., Shi, X., Shi, Z., Benfatto, L. & Popović, D. Effective two-dimensional thickness for the Berezinskii-Kosterlitz-Thouless-like transition in a highly underdoped $La_{2-x}Sr_xCuO_4$. *Phys. Rev. B* **93**, 024519 (2016).
60. Guo, J. G. et al. Quasi-two-dimensional superconductivity from dimerization of atomically ordered $AuTe_2Se_{4/3}$ cubes. *Nat. Commun.* **8**, 871–871 (2017).
61. Mondal, M. et al. Role of the vortex-core energy on the berezinskii-kosterlitz-thouless transition in thin films of NbN. *Phys. Rev. Lett.* **107**, 217003 (2011).
62. Veyrat, A. et al. Berezinskiikosterlitz–thouless transition in the type-I weyl semimetal $PtBi_2$. *Nano Lett.* **23**, 1229–1235 (2023).
63. Nizhankovskiy, V. I. & Rogacki, K. BKT transition observed in magnetic and electric properties of $YBa_2Cu_3O_{7-\delta}$ single crystals. *Phys. Rev. B* **100**, 104510 (2019).
64. Yano, R. et al. Evidence of unconventional superconductivity on the surface of the nodal semimetal $CaAg_{1-x}Pd_xP$. *Nat. Commun.* **14**, 6817 (2023).
65. Kuibarov, A. et al. Evidence of superconducting Fermi arcs. *Nature* **626**, 294–299 (2024).
66. Gofryk, K. Local inhomogeneity and filamentary superconductivity in Pr-doped $CaFe_2As_2$. *Phys. Rev. Lett.* **112**, 047005 (2014).
67. Lee, K. et al. Discovery of a weak topological insulating state and van Hove singularity in triclinic $RhBi_2$. *Nat Commun* **12**, 1855 (2021).
68. Sanchez, D. S. et al. Tunable topologically driven Fermi arc van Hove singularities. *Nat. Phys.* **19**, 682–688 (2023).
69. Cao, Y. et al. Unconventional superconductivity in magic-angle graphene superlattices. *Nature* **556**, 43–50 (2018).
70. Namba, R. et al. Two-step growth of high-quality single crystals of the Kitaev magnet *a*–$RuCl_3$. *Phys. Rev. Mater.* **8**, 074404 (2024).
71. Kresse, G. & Furthmüller, J. Efficient iterative schemes for ab initio total-energy calculations using a plane-wave basis set. *Phys. Rev. B* **54**, 11169 (1996).
72. Perdew, J. P., Burke, K. & Ernzerhof, M. Generalized gradient approximation made simple. *Phys. Rev. Lett.* **77**, 3865 (1996).
73. Mostofi, A. et al. wannier90: a tool for obtaining maximally-localised Wannier functions. *Comput. Phys. Commun.* **178**, 685–699 (2008).
74. Marzari, N. & Vanderbilt, D. Maximally localized generalized Wannier functions for composite energy bands. *Phys. Rev. B* **56**, 12847 (1997).
75. Wu, Q., Zhang, S., Song, H.-F., Troyer, M. & Soluyanov, A. A. Wanniertools: An open-source software package for novel topological materials. *Comput. Phys. Commun.* **224**, 405 (2018).
76. Sancho, M. P. L., Sancho, J. M. L. & Rubio, J. Highly convergent schemes for the calculation of bulk and surface green functions. *J. Phys. F Metal. Phys.* **15**, 851 (1985).

Acknowledgements

We thank Sougata Mardanya, Carmine Autieri, Ruixing Zhang, and Titus Neupert for illuminating discussions. M.Z.H.'s group acknowledges primary support from the Gordon and Betty Moore Foundation for the experimental work. R.I. and F.X. acknowledge the support by the National Science Foundation under Grant No. OIA-2229498. R.I. and F.X. acknowledge the access to the computing facility Cheaha at the University of Alabama at Birmingham. L.B. is supported by DOE-BES through the award DE-SC0002613. Z.M. acknowledges the National Natural Science Foundation of China (grant no. 62150410438) and Beihang University, Hangzhou Innovation Research Institute Fund (20241216100100022905 8). The National High Magnetic Field Laboratory (NHMFL) acknowledges support from the US-NSF Cooperative agreement Grant number DMR-DMR-2128556 and the state of Florida. Z.G. acknowledges support from the Swiss National Science Foundation (SNSF) through the SNSF Starting Grant (no. TMSGI2_211750). The muon spin relaxation experiments were carried out at the Swiss Muon Source (SμS), Paul Scherrer Institute (Villigen, Switzerland), using the FLAME (FLexible and Advanced MuSR Environment) instrument. We thank T. Murphy, G. Jones, L. Jiao, and R. Nowell at NHMFL for their technical support. M. K. would like to thank the Sharif University of Technology and INSF-Grant No. 4027770.

Author contributions

M.S.H. conceived the project. Electrical transport experiments were performed by M.S.H. and Q.Z. in consultation with L.B. Photoemission spectroscopy measurements were performed by Z.J.C. in consultation with M.S.H, X.P.Y., B.K, and T.A.C. Crystal growth was carried out by Z.M. and W.Z. Theoretical calculations were performed by R.I., I.E.P., F.X., and M.K. Muon spin relaxation measurements were carried out by Z.G., J.A.K., T.H., and H.L. Figure development and writing of the paper were undertaken by M.S.H., L.B., Z.J.C., R.I., Z.M., and M.Z.H. M.Z.H. supervised the project. Y.X.J., M.L., and B.C. helped in setting up measurements.

Competing interests

The authors declare no competing interests.

Additional information

Supplementary information The online version contains supplementary material available at https://doi.org/10.1038/s41467-025-58024-w.

Correspondence and requests for materials should be addressed to Md Shafayat Hossain or M. Zahid Hasan.

Peer review information *Nature Communications* thanks the anonymous reviewers for their contribution to the peer review of this work. A peer review file is available.